Facile Approach for Synthesizing High-Performance MnO/C Electrodes from Rice Husk

Zhan, Dan; Luo, Wei; Kraatz, Heinz Bernhard; Fehse, Marcus; Li, Yuqi; Xiao, Zuoan; Brougham, Dermot F.; Simpson, André J.; Wu, Bing

Facile Approach for Synthesizing High-Performance MnO/C Electrodes from Rice Husk

Dan Zhan,*,†,‡ Wei Luo,† Heinz-Bernhard Kraatz,§ Marcus Fehse,⊥,∥ Yuqi Li,† Zuoan Xiao,†,‡ Dermot F. Brougham,# André J. Simpson,§ and Bing Wu*,§,∥

†College of Food Science & Chemical Engineering, Hubei University of Arts and Science, Xiangyang 441053, P. R. China

‡Hubei Key Laboratory of Power System Design and Test for Electrical Vehicle, Xiangyang 441053, P. R. China

§Department of Physical and Environmental Sciences, University of Toronto Scarborough, Toronto M1C 1A4, Canada

∥Dutch-Belgian Beamline (DUBBLE), ESRF—The European Synchrotron Radiation Facility, CS 40220, Grenoble Cedex 9 38043, France

⊥Faculty of Applied Sciences, Delft University of Technology, Mekelweg 5, Delft 2628 CD, the Netherlands

#School of Chemistry, University College Dublin, Belfield, Dublin 4 D04 V1W8, Ireland

Ⓢ Supporting Information

ABSTRACT: Pyrolysis is an effective way to convert biomass into biofuel while obtaining highly porous active carbon materials. In this study, a facile approach, involving hydrothermal and pyrolysis steps, is described for preparing hybrid metal oxide nanoparticle-embedded porous hard carbon matrices (MnO/C) from the biowaste rice husk and organometallic precursors. It was found that the pyrolysis/calcination temperature had a strong influence over the microstructure, especially over the porosity, but also over the carbon content and crystallinity of the nanocomposites; hence, the electrical properties can be controlled. Galvanostatic measurements showed that the nanocomposite obtained at 600 °C exhibited the highest charge/discharge capacity and best stability, delivering an initial discharge capacity of 1104 mA·h·g^{-1} at a current density of 200 mA·g^{-1}, and retaining a value of 830 mA·h·g^{-1} after 200 cycles, suggesting excellent cycle stability. A discharge capacity of 581 mA·h·g^{-1} was obtained even at a current density as high as 2400 mA·g^{-1}, demonstrating superb rate capability. This outstanding electrochemical performance, ascribed to high electrochemical activity of the embedded MnO nanoparticles enhanced by electrical conductivity provided through the high surface area of the active porous carbon support, is discussed in relation to the microstructure of the nanocomposite.
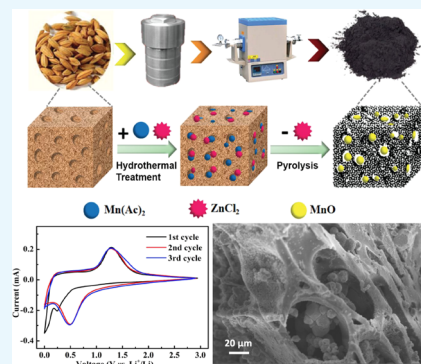
1. INTRODUCTION

Increasing environmental awareness and demand for green energy resources have resulted in the burgeoning field of energy storage materials.[1−3] For instance, lithium ion batteries (LIB) have attracted huge attention because of their high energy density, low self-discharging, and the absence of any memory effects.[4] Ultimately, the electrochemical performance of the LIB system is dependent on the electrodes used; however, conventional graphite anodes are not capable of supporting next-generation LIB as they typically have low theoretical capacity (372 mA·h·g^{-1}).[5] Hence, there has been significant focus on developing LIB systems using new anode materials with high capacity and stable response over multiple cycles.[6−8] Among these, pioneering work by Poizot et al. demonstrated huge potential for using transition-metal oxide (M_xO_y, M = Ni, Co, Cu, and Fe) anodes, which can achieve capacities up to 1000 mA·h·g^{-1}, and have larger volume specific capacity by an order of magnitude than conventional carbon anode materials.[6] As a consequence, this approach has since been extensively explored.[9−13]

Manganese oxide (MnO), a transition-metal oxide, is considered to be a promising anode material as it has a high theoretical capacity (755 mA·h·g^{-1}). However, it normally suffers from poor rate performance and low long-term cycle tolerance, arising from low electrical conductivity and large volume changes during electrochemical cycling.[9,14] It is known that morphological nanostructuring of the oxides can facilitate Li$^+$ ion transport and increase the electrode/electrolyte contact area.[10] Thus, in an effort to improve electrochemical performance, electrode materials with various morphologies like microcages,[11] hollow spheres,[15] or porous[16] structures have been reported. Although these improvements enhance the rate performance, they do not solve the problem of long-term cycling performance caused by self-aggregation of MnO nanostructure during cycling.

On the other hand, carbon materials offer the advantages of good electronic conductivity, structural flexibility, and can be

sourced from a wide range of materials; hence, they have considerable potential for designing novel composite materials. Anodes made of MnO−carbon composites (MnO/C) provide high electrode capacity, while also effectively stabilizing the structure (restraining volume changes during charge/discharge) improving long-term cycling and rate performance.[17−19] Composites have been synthesized from graphene,[20] carbon nanotubes,[21] and organic compounds[22] using hydrothermal reactions[23] or pyrolysis.[24] Hence, several MnO/C anodes with excellent electrochemical performance synthesized for LIB systems have been reported over the last decade.[11,22,23,25] For instance, Ding et al. constructed a MnO/C composite from graphite using a facile hydrothermal reaction, while having excellent cycling stability, it also retained a capacity of 497 mA·h·g^{-1} after 120 cycles.[20] Yolk−shell MnO/C nanodiscs were prepared by Xiao et al. via a carbothermal reaction from polydopamine, in which a high reversible capacity of 910 mA·h·g^{-1} at 0.1 A·g^{-1} was retained even after 600 cycles.[26]

As a byproduct of rice production, rice husk accounts for a worldwide output of approximately 140 million tons per year.[27] In most countries, rice husk is either disposed of as waste or burnt. However, because of its porous nature, rice husk has very low density, making it bulky and expensive to transport, whereas the ash produced from burning can cause significant environmental issues if directly dumped.[28] Hence, there is a strong need to develop new industrial processes that convert the rice husk biomass from a problematic waste to a high value commodity. Thus, various avenues for its recycling have been explored including use as a carbon source for catalysts, supports, membranes, and nanocomposite materials.[29−32] Biomass-derived carbon materials, especially those embedded with transition-metal oxide nanoparticles, have been frequently used as electrode materials in battery/supercapacitor systems.[33−36] Interestingly, Liu et al. reported a (metal-free) hierarchical porous carbon material formed by carbonization of rice husk, which showed excellent electrochemical properties with high capacitance (278 F·g^{-1} at 0.5 A·g^{-1}) and rate capability (77.2% retention of capacitance at 20 A·g^{-1}).[37] Hence, it is expected that rice husk-derived hierarchical porous structures could provide a matrix with excellent electrochemical properties, which also acts as effective supports for metal oxide nanoparticles, preventing their aggregation during electrochemical cycling, which would in turn help improve lithium storage. Recently, a study by Yuan et al. used MnO$_2$/rice husk-derived carbon (MnO$_2$/RHC) as anode materials for supercapacitors, in which enhanced electrochemical performance was indeed observed.[38] However, most of the MnO/C composites reported were prepared through heat treatment of their precursors in an ex situ process, which reduces the porous area accessible to embedding nanoparticles.

In this study, porous MnO/C composite materials were constructed in situ from rice husk through a facile process involving a hydrothermal treatment followed by pyrolysis. The carbon support prepared was found to inherit the hierarchical porous structure from rice husk, whereas MnO nanoparticles were simultaneously formed inside these pores by the calcination process. Benefiting from this hierarchical porous structure, the MnO/C composite material exhibited much better lithium storage performance than pristine MnO. The effect of pyrolysis temperature on the structure, composition, and electrochemical properties of the nanocomposites was also

investigated in detail. It was found that the MnO/C nanocomposite formed at 600 °C exhibited optimal electrochemical performance as an anode material for LIBs. Given the low cost of the biomass, the ease of production of the composite, and the excellent electrochemical performance, we suggest that the approach described here has significant potential for electrochemical applications including high-power LIBs.

2. RESULTS AND DISCUSSION

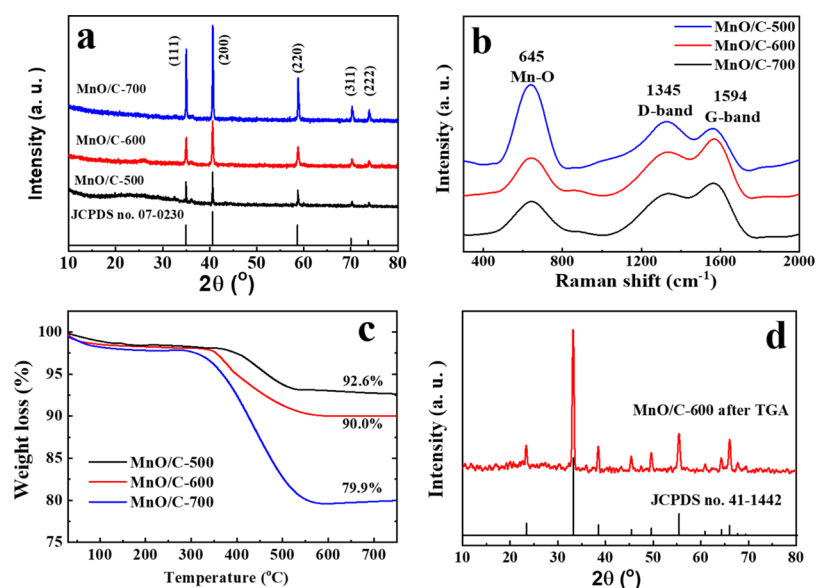**2.1. Formation and Characterization of MnO/C Nanocomposites.** The synthesis of porous MnO/C composite material using a hydrothermal process followed by concurrent pyrolysis is illustrated in Figure 1, full details are
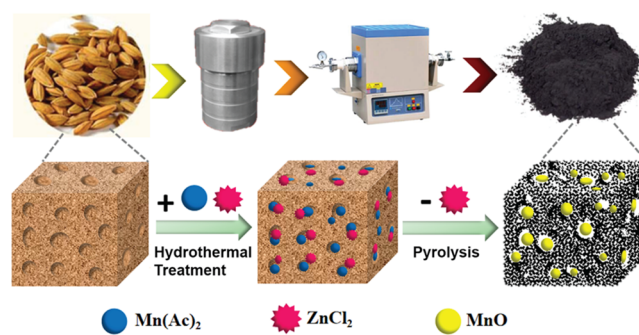
Figure 1. Schematic diagram of the fabrication of porous MnO/C nanocomposite from rice husk using hydrothermal treatment followed by pyrolysis under anaerobic conditions.

given in Section 4.1. During the hydrothermal synthesis, Mn(Ac)$_2$ and ZnCl$_2$ solutions permeate throughout the rice husk pores. Heating of this material under anaerobic conditions results in the formation of MnO nanoparticles and the rice husk is carbonized to porous carbon with most organic components lost as volatile low-molecular-weight molecules. It is well known that the organic acid roots of Mn(Ac)$_2$ under high temperature and inert atmosphere would undergo a decomposition to form H$_2$O, CO/CO$_2$, and MnO, a stable oxidized form of Mn.[4] On the hand, ZnCl$_2$ can act as a catalyst to initiate the dehydroxylation and dehydration reactions, which convert hydrogen and oxygen in the biomass material into water vapor, and result in the production of porous structure.[39,40] ZnCl$_2$ is subsequently removed by copious washing with diluted hydrochloride acid and water to yield an MnO/C composite material with a hierarchical porous structure.

Figure 2a shows the X-ray powder diffraction (XRD) patterns of MnO/C samples calcined at 500, 600, and 700 °C together with the reference diffraction pattern of cubic MnO. The powder diffraction patterns are virtually identical, indicating the presence of crystalline cubic MnO embedded within the carbon matrix. The diffraction peaks at 2θ = 35, 40, 59, 70, and 74° are readily indexed to the (111), (200), (220), (311), and (222) crystal planes of cubic MnO with an $Fm3m$ space group (JCPDS no. 07-0230). A similar conclusion about the formation of MnO can be found from X-ray photoelectron spectroscopy (XPS) analyses (see Supporting Information). It is interesting to note that the intensity of the features increases with an elevated pyrolysis temperature (similar masses and acquisition times were used in each case), suggesting improved crystallinity of the product. The absence of diffractions

Figure 2. Physical characterization of MnO/C nanomaterials prepared at 500, 600, and 700 °C: (a) XRD patterns of the three MnO/C materials together with a standard (cubic MnO), (b) their Raman spectra indicating the typical D and G bands of carbon materials, and (c) TGA profiles recorded between 30 and 750 °C in air for MnO/C-500, 600, and 700; (d) XRD pattern of MnO/C-600 recorded after TGA.

corresponding to carbon and silica materials confirms that the rice husk-derived matrices are predominantly composed of amorphous carbon.[37] In the case of MnO/C-500, a broad signal at $2\theta = 23°$ may be arise from reflections of the (002) crystal plane of carbon.[41]

The carbon matrix was further analyzed by Raman spectroscopy; the features observed at 1345 and 1594 cm^{-1} correspond to sp^3-bonded structure carbon (D-band) and sp^2-bonded graphitized carbon (G-band), respectively.[42] The intensity ratio of these bands (I_D/I_G) can be used to evaluate the disorder of biomass-derived carbon; a lower I_D/I_G value corresponding to a higher degree of graphitization. Analysis of the spectra shown in Figure 2b, provides I_D/I_G values of 1.26, 0.91, and 0.88 for MnO/C-500, -600, and -700, respectively, suggesting that MnO/C-700 possesses the most ordered graphitic carbon. As graphitization is usually associated with reduced concentration of lattice defects, which is beneficial for electron transport and ultimately for electronic conductivity, higher temperatures may be favorable. Temperature may also affect the inorganic component of the nanocomposite. The signal observed at 645 cm^{-1} can be assigned to the MnO vibration, and its linewidth can be related to the MnO nanoparticle size;[43] for the samples studied here, the broader linewidth of this signal in MnO/C-600 suggests that it contains the smallest MnO nanoparticles.

The carbon content of the samples was measured by thermogravimetric analyses (TGA) performed in air. As shown in Figure 2c, a small weight loss (~2%) below 100 °C was observed for all samples, which can be attributed to the evaporation of adsorbed water from the surfaces. From 300 to 700 °C, the change in mass corresponds to the oxidation of MnO to Mn_2O_3, as well as to carbon loss because of the formation of CO_2 gas.[44,45] The XRD pattern of the residual MnO/C-600 sample after TGA analysis, shown in Figure 2d, is identical to Mn_2O_3 (JCPDS no. 41-1442). Assuming quantitative oxidation from MnO to Mn_2O_3 and no loss of Mn content, the carbon content in the materials can be calculated to be 28.3, 18.9, and 16.8% for MnO/C-500, -600, and -700, respectively, demonstrating increasing loss of matrix

as the pyrolysis/calcination temperature is increased, as expected.

The morphology and microstructure of MnO/C-600 was studied in greater detail by scanning electron microscopy (SEM) and transmission electron microscopy (TEM). As clearly visible in the SEM images shown in Figure 3a−c, the carbon matrix possesses a complex structure with pore sizes varying over a wide size range as inherited from the raw rice husk material (see Figure S3). An example of multiscale porosity can be observed in Figure 3b, where micropores can
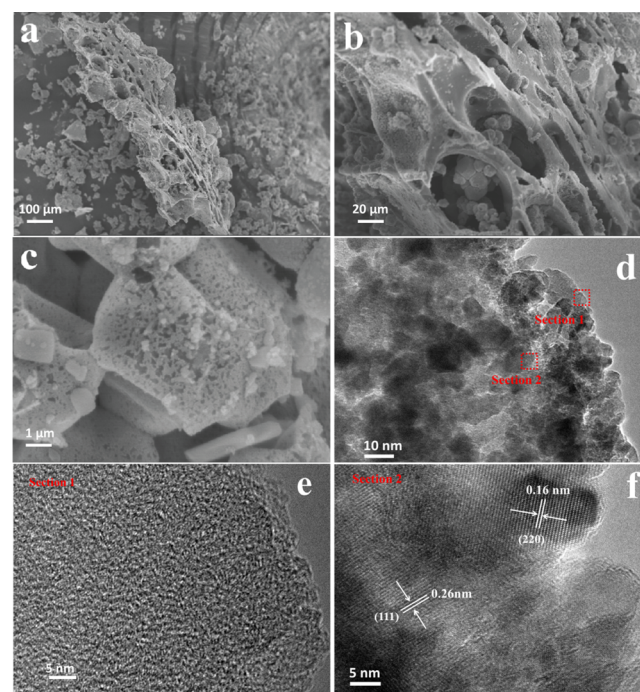
Figure 3. Electron microscopy studies of MnO/C-600. SEM images (a−c) and TEM image (d) of MnO/C-600; (e,f) HRTEM images of MnO/C-600 corresponding to the sections in (d), respectively.
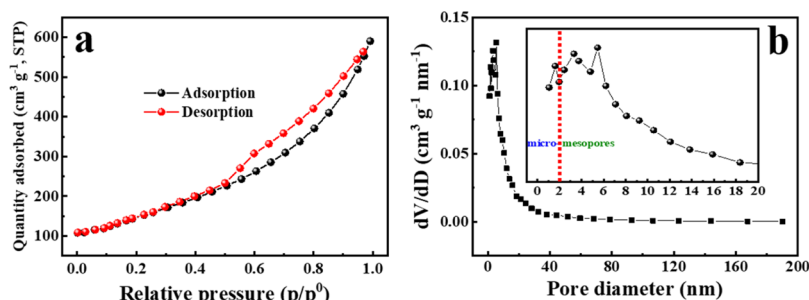
Figure 4. (a) N_2 adsorption−desorption isotherms, and the (b) corresponding pore size distribution for MnO/C-600.

be observed on the inner walls of macropores. It is generally accepted that the porous structure is a result of the loss of volatiles such as H_2O and CO_2 from the scaffold during pyrolysis.[46] Large numbers of quasispherical features, with a diameter of *ca.* 100 nm, are apparent at this magnification, which are attributed to MnO nanoparticles attached to the surface of the porous carbon. In the magnified SEM image (Figure 3c), these features of small holes, with an average diameter of 40 nm, are apparently covered with MnO particles. On the other hand, those observed quasispherical carbon microspheres can be produced by the dehydration/polymerization/condensation of low-molecular-weight saccharides from the biomass during the hydrothermal process.[47] Moreover, TEM images (Figure 3d) of microtomed samples confirm that the distribution of MnO particles on the surface of the porous carbon matrix is not uniform. High-resolution TEM (HRTEM) images reveal no distinguishable lattice fringes for graphitic carbon, despite extensive scanning (a typical image is shown in Figure 3e). This is consistent with the XRD and Raman studies which demonstrate largely amorphous carbon. On the other hand, the HRTEM images (Figure 3f) of areas containing MnO nanoparticles display clear lattice fringes for crystalline MnO, that is, the (111) and (220) crystal planes with lattice spacings of 0.26 and 0.16 nm, respectively.

To measure the porosity of MnO/C-600, isothermal N_2 adsorption−desorption studies were undertaken. The adsorption−desorption isotherm demonstrates a type IV isotherm with a H3 type hysteresis loop (Figure 4a).[45] The desorption−adsorption hysteresis occurred over relative pressures (p/p^0) from 0.4 to 0.9 and can be attributed to the capillary condensation, because of the presence of mesopores. Additionally, a rapid increase in adsorption at high relative pressure ($p/p^0 > 0.9$) suggests the presence of a significant fraction of macropores in the hybrid, as indicated in SEM images. The pore size distribution curves were calculated using the Barrett−Joyner−Halenda method; the result for MnO/C-600 is shown in Figure 4b. Although significant polydispersity was apparent, the average pore size in MnO/C-600 was 42 nm, which again is consistent with that observed by SEM, which suggests the images are representative of the sample. The N_2 adsorption specific surface areas of MnO-500, 600, 700, and the MnO standard were found to be 681, 953, 1009, and 511 $m^2 \cdot g^{-1}$, respectively.

2.2. Electrochemical Performance of MnO/C Nanocomposites.

Cyclic voltammetric (CV) analyses of MnO/C-600 was undertaken in the voltage range from 0.01 to 3.0 V at a scan rate of 0.1 $mV \cdot s^{-1}$. Figure 5 shows the first three successive scans. In the first cycle, the cathodic peak at around 0.26 V is assigned to the initial reduction of MnO to metallic Mn ($MnO + 2Li^+ + 2e^- \rightarrow Mn + Li_2O$), and the formation of
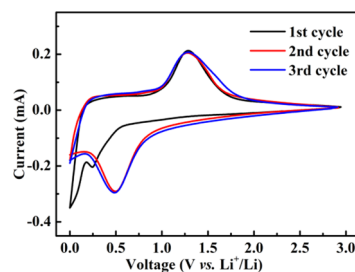
Figure 5. CV curves of MnO/C-600 in the range of 0.01−3.0 V at a scan rate of 0.1 $mV \cdot s^{-1}$ vs Li^+/Li.

a solid electrolyte interface (SEI). The sharp peak at a lower voltage can be attributed to the intercalation of Li into the graphite layer at 0.05 V.[20] The anodic peak at 1.26 V is ascribed to MnO formation ($Mn + Li_2O \rightarrow MnO + 2Li^+ + 2e^-$), and decomposition of Li_2O.[48] The subsequent cycles differ from the first cycle because of irreversible nanosizing and restructuring of the electrode.[49,50] The reduction peak is found to shift to ca. 0.5 V, whereas the oxidation peak is still observed at 1.26 V, suggesting an irreversible phase transformation.[51] This transformation induces a decrease in the separation between the reduction and oxidation peaks (ΔU), which indicates weaker polarization and better reversibility because of the higher electronic conductivity of carbon support after the nano-restructuring.[52] The CV curves were stable to further cycling.

In Figure 6a, the voltage profiles of the initial charge/discharge curves of the three samples and MnO in the potential range from 0.01 to 3.0 V at a current density of 100 $mA \cdot g^{-1}$ are presented. All samples exhibit the same discharge plateau at about 0.26 V, which we attribute to the reduction of Mn(II) to Mn(0) during lithiation. The charge plateau was found at *ca.* 1.26 V, which we assign to the oxidation of Mn(0) to Mn(II) during delithiation.[53] The steep slope of the curves before the discharge plateau (~0.26 V) suggests a significant capacity loss, presumably as a result of irreversible electrolyte decomposition, and as a result almost a third of the inserted charge cannot be retrieved. Such effects can result in the formation of an SEI layer and the occupation of irreversible surface sites by Li within the carbon matrix.[54,55] However, for applications, the addition of additives, for example $LiPF_6$,[56] into the carbon matrix can mitigate such effects. MnO/C-500, 600, and 700 delivered initial discharge capacities of 1196, 1326, and 1238 $mA \cdot h \cdot g^{-1}$, respectively. This is significantly higher than the initial discharge capacity of MnO (756 $mA \cdot h \cdot g^{-1}$); we suggest that this is because of the strong interaction between the MnO phase and the porous carbon phase[57] as well as the elevated specific surface area.[58] We suggest that the low
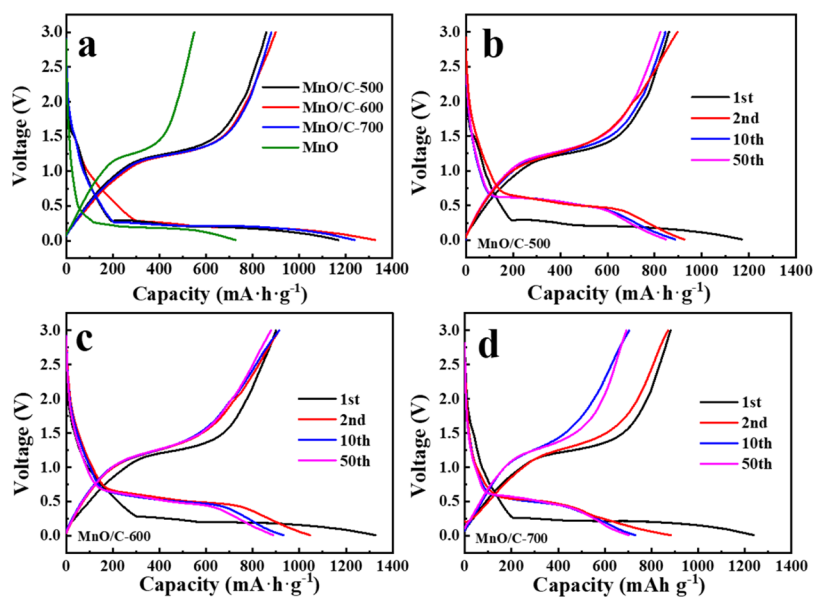
Figure 6. (a) First charge/discharge curves of MnO/C-500, 600, 700, and MnO; (b) charge/discharge voltage profiles of MnO/C-500; (c) MnO/C-600, and (d) MnO/C-700 for different cycles at 100 mA g^{-1}.

capacity of MnO/C-500 may be connected to the low MnO crystallinity and that any beneficial effect of high crystallinity for MnO/C-700 is offset by the rather low carbon content (16.8%). MnO/C-600 with intermediate carbon content and crystallinity displayed the highest discharge capacity. The Coulombic efficiencies of the three samples are similar with values of 70.2, 69.7, and 71.3% measured for MnO/C-500, -600, and -700, respectively. The low, similar Coulombic efficiency is mainly related to the irreversible conversion reaction and formation of an SEI film in all cases, as it frequently occurs in metallic oxide-based anodes.[6]

The charge/discharge voltage profiles with different cycles for the three materials MnO/C-500, 600, and 700 are shown in Figure 6b−d, respectively. The profiles are quite similar; a prominent voltage plateau is located at around 0.5 V after the first cycle for each sample, implying irreversible restructuring and nanosizing of the electrode material upon initial discharge. Although, for all the materials, the discharge capacity of the second cycle is drastically reduced, their charge capacity only decreases slightly, resulting in a strong increase of Coulombic efficiency to more than 98%. The capacity loss is most pronounced for MnO/C-700 (from 1238 to 890 mA·h·g^{-1}) after the initial charge/discharge cycle, presumably as a result of its larger specific surface area, which promotes continuous electrolyte degradation and SEI formation that in turn hampers charge storage.[51]

The cycling performance of the four materials, at a current density of 200 mA·g^{-1}, are shown in Figure 7a. Distinct capacity decay can be observed, especially during the first 60 cycles for MnO/C-500 and -600, whereas the capacity for MnO/C-700 reduced more steadily. The high crystallinity and large surface area of MnO/C-700 is presumably responsible for better initial capacity retention.[59,60] On further cycling, the capacity for MnO/C-500 and -600 was observed to decrease steadily, and that for MnO/C-700 decayed drastically to be almost equal to that of MnO/C-500 by around the 180th cycle. We suggest that the high specific surface area of MnO/C-700, which promotes continuous SEI formation, is the principle cause of decaying capacity with prolonged cycling.
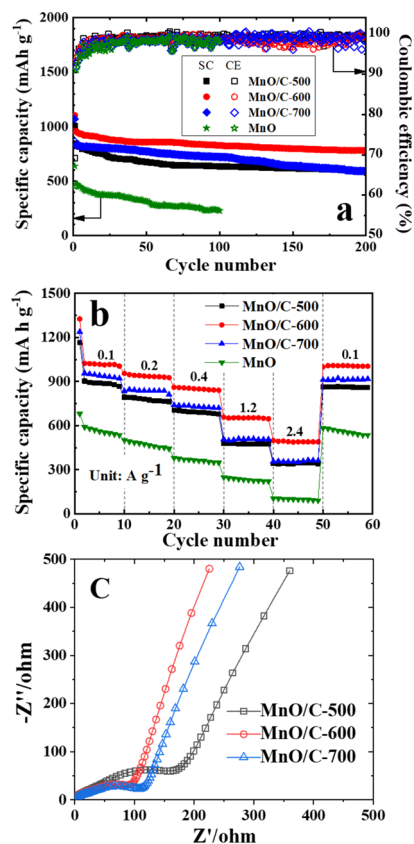
Figure 7. Electrochemical cycling of MnO/C-500, -600, and -700; (a) rate performance; (b) cycling performance at a current rate of 200 mA g^{-1}; (c) Nyquist representation of electrochemical impedance response spectrum.

MnO/C-600 maintained the highest specific capacity of 830 mA·h·g^{-1} after 200 cycles, whereas values of 621 and 593 mA·h·g^{-1} were obtained for MnO/C-500 and -700, respectively. In comparison with the composites, the capacity of pure MnO

Table 1. Comparison of Electrochemical Performance of the as-Obtained MnO/C Composite Anode Material with Performance of Previously Reported Similar Electrode Materials

composite	initial capacity/mA·h·g⁻¹ (current density/mA·g⁻¹)	capacity retention/mA·h·g⁻¹ (cycle number, current density/mA·g⁻¹)	rate capability/mA·h·g⁻¹ (current density/mA·g⁻¹)	carbon source	refs
MnO/C microcage	1063 (100)	1451 (270, 100)	236 (5000)	agar	11
porous MnO/C nanotube	1129 (100)	763 (100, 100)	303 (3143)	alcohol	16
porous MnO@C	2020 (100)	1159 (50, 100)	252 (800)	MOF	22
porous MnO/C microspheres	1022 (100)	702 (50, 100)	230 (3000)	microalgae	51
MnO−graphene core−shell nanowires	1385 (50)	886 (500, 1000)	508 (3000)	graphene	67
hierarchical MnO@C microspheres	1691 (100)	596 (1000, 3825)	380 (3800)	MOF	68
cauliflower-like MnO@C/N	961 (500)	837 (300, 500)	394 (4000)	L-tryptophan	69
lotus root-like MnO/C	1410 (750)	1084 (250, 750)	462 (3770)	$H_2C_2O_4$	70
porous MnO/C	1080 (98)	629 (300, 997)	314 (3143)	PEG6000	25
porous MnO/C	1573 (100)	1691 (200, 100)	630 (1600)	glucose	44
MnO/C	1080 (100)	1625 (1000, 1000)	483 (5000)	alginate	71
MnO/C core−shell nanowire	1179 (100)	903 (100, 100)	483 (2000)	PPy	23
MnO/C	1072 (50)	740 (50, 100)	436 (3000)	pollen grains	72
yolk−shell MnO@C	1347 (100)	605 (600, 1000)	248 (5000)	dopamine	26
mesoporous MnO/C	1456 (200)	1224 (200, 200)	-	ethylene glycol	54
MnO/C nanopeapods	1018 (500)	525 (1000, 2000)	463 (5000)	PDA	53
MnO/C core−shell nanorods	1090 (200)	600 (40, 200)	-	F127	73
MnO@C core−shell nanoplates	1365 (200)	563 (30, 200)	500 (300)	C_2H_2	55
MnO/C	1326 (100)	830 (200, 200)	581 (2400)	rice husk	this

decreased rapidly upon cycling because, presumably, of the absence of a supporting matrix.

The rate capabilities of the four samples were investigated at different current densities, increasing stepwise from 0.1, 0.2, 0.4, 1.2, 2.4 A·g⁻¹ for every 10th cycle, and then decreasing to 0.1 A·g⁻¹, as shown in Figure 7b. The discharge capacity of all the samples decreased gradually with increasing current density, suggesting diffusion-controlled kinetics for the electrode reaction.[61] After a significant decay in the second cycle, the capacities of all three samples were relatively stable, even at current densities as high as 2.4 A·g⁻¹. Note that the initial discharge capacity at 0.1 A·g⁻¹ was essentially recovered when the current density was reset to 0.1 A·g⁻¹ after the full cycle. It was also found that the observed initially gradual decrease in capacity weakened progressively with the charge/discharge cycle (irrespective of the current density). For MnO/C-500 and -700, this process was completed by the 30th to 50th cycle, and a little later for MnO/C-600. This is also the highest performing nanocomposite; apparently it has the best balance between MnO content and porous carbon support. As noted above, increased surface area of the support apparently promotes electrolyte decay and SEI formation, with detrimental effects on cycling response.[51] However, even at current density as high as 2.4 A·g⁻¹, MnO/C-600 still delivered a capacity of 581 mA·h·g⁻¹, far exceeding the value of pure MnO (97 mA·h·g⁻¹). After charging/discharging 60 cycles successively (Figure 7b), MnO/C-600 retained 43% of the initial capacity, whereas MnO/C-500, -700, and MnO only retained 35, 26, and 15%, respectively. Evidently, the excellent rate capability of the hybrid material is dependent on the high surface area of porous carbon, which improves electron conductivity,[62] while it is also providing an open framework

with short lithium diffusion paths,[10] and acts as a strong support to maintain the structural integrity of the nanoscale metal oxide nanoparticles over hundreds of lithiation/delithiation cycles.

To understand the differences in electrochemical performance of the nanocomposites, electrochemical impedance spectroscopy (EIS) measurements were undertaken. The Nyquist plots measured for the electrodes are shown in Figure 7c. It is well-known that a semicircular response in the mid-frequency range corresponds to the charge transfer impedance (R_{ct}) at the electrode/electrolyte interface, whereas the upward trajectory inclined line at the low-frequency range relates to lithium ion diffusion.[63] The diameter of the arched profile for the MnO/C-600 electrode is the smallest among the three, indicating the smallest charge transfer impedance.[64] MnO/C-600 has lower graphitization degree than MnO/C-700, but it has higher carbon content with better conductivity. Consequently, MnO/C-600 displayed the smallest R_{ct} in the EIS tests.

Therefore, the overall evaluation of the impact of pyrolysis temperature on the lithium storage performance showed that the composite obtained at 600 °C exhibited the best electrochemical performance. It has been reported that metal oxide nanocomposite electrodes with increased carbon content and crystallinity raise the charge transfer resistance,[65,66] whereas elevated surface area is known to accelerate electrolyte decay.[51] As a consequence, MnO/C-600 displayed the best rate performance, as it represents the best compromise in terms of carbon content, crystallinity, and specific surface area, leading to superior electrochemical performance and the smallest charge-transfer resistance. There are many reports of MnO/C composites for LIB anode applications for which

many carbon sources were used. In Table 1 the electrochemical performance of as-obtained MnO/C materials from recent studies are presented. In most cases, the source was low-molecular-weight organic substances (e.g. ethanol, L-tryptophan, ethylene glycol) along with a few natural products (e.g. microalgae, pollen grains). Rice husk, as a major biomass waste, has long been considered as an excellent alternative cheap carbon source. Compared to other listed composite materials, the MnO/C rice husk-derived nanocomposite reported here displays an outstanding performance; with initial discharge capacity of 1326 mA·h·g^{-1} (at 100 mA·g^{-1}) measured, along with discharge capacities of 830 mA·g^{-1} (at 200 mA·g^{-1} after 200 electrochemical cycles) and of 581 mA·h·g^{-1} (at high current density of 2400 mA·g^{-1}), demonstrating excellent cyclability and rate capability.

3. CONCLUSIONS

In summary, MnO/C nanocomposites were successfully prepared using biomass rice husk as the carbon source by a simple hydrothermal process followed by pyrolysis. During the in-situ preparation, a hierarchical porous structure inherited from rice husk was formed and MnO particles were simultaneously created and embedded onto the walls of these pores. The evaluation of the impact of pyrolysis temperature on the lithium storage performance found that the composite obtained at 600 °C exhibited the best electrochemical performance. An initial discharge capacity of 1326 mA·h·g^{-1} at a current density of 100 mA·g^{-1} was observed for this composite, along with a discharge capacity of 830 mA·h·g^{-1} at a current density of 200 mA·g^{-1} after 200 electrochemical cycles, indicating reliable cycle performance. A discharge capacity of 581 mA·h·g^{-1} was also delivered even at a high current density of 2400 mA·g^{-1}, demonstrating excellent rate capability. We suggest that the hierarchical porous structure of the carbon framework, the highly crystalline MnO content, and strong interactions between the inorganic and organic phases owing to intimate contact arising from in situ particle formation are responsible for this excellent electrochemical performance. In view of the facile preparation method and excellent electrochemical performance, the approach described above enables the optimization of electrode performance for LIBs and other energy storage applications via a sustainable path involving re-utilization and recycling of waste biomass.

4. EXPERIMENTAL SECTIONS

4.1. Synthesis of MnO/C Composites.
Zinc chloride (ZnCl$_2$), ethanol (95 wt %), manganese acetate tetrahydrate (Mn(Ac)$_2$·4H$_2$O), hydrochloride acid (37 wt %), N-methyl pyrrolidone (NMP), polyvinylidene fluoride (PVDF), and acetylene black were purchased from Sinopharm Chemical Reagent Co. Ltd. (China). Rice husks were acquired from a local market (Xiangyang, China), and pretreated with 10 wt % NaOH aqueous solution at 100 °C to remove silica and other impurities [as demonstrated in Si 2p XPS spectrum (Figure S2)].[38] All other chemical reagents were of analytical grade and used without further treatment. In a typical process, the rice husks were ground into powder and washed with distilled water and ethanol repeatedly five times, and then the powder was dried in the air at 120 °C overnight. Afterward, 1.73 g of the dried clean husk powder was immersed into 200 mL 0.1 mol·L^{-1} Mn(Ac)$_2$ solution containing 1.73 g of ZnCl$_2$. The above mixture was transferred to a Teflon-lined stainless autoclave and hydrothermally treated at 140 °C for 10 h. After cooling to room temperature, the mixture was freeze-dried and then heated inside a tube furnace under argon atmosphere at a high temperature for 4 h and cooled naturally. Next, the solid residue was washed repeatedly with 0.1 mol·L^{-1} HCl solution and then deionized water, to remove ZnCl$_2$. After the washing step, the sample was dried at 120 °C for 10 h. To compare the effect of pyrolysis temperature on the electrochemical performance of the carbon materials, the samples were heated to 500, 600, and 700 °C, providing three MnO/C composites, labeled as MnO/C-500, -600, -700, respectively. For comparison, MnO particles were obtained by calcination of Mn(Ac)$_2$·4H$_2$O at 600 °C under argon atmosphere.

4.2. Material Characterization.
All phase identification of composite materials reported in this contribution was conducted using a Bruker D8 ADVANCE X-ray diffractometer with Cu Kα radiation (λ = 0.15418 nm). Raman spectra were acquired using 523 nm line of Ar-ion Laser as excitation source by a Raman microscope (Renishaw, InVia, England). The carbon content in the samples was measured by thermogravimetric analysis using a thermogravimetric instrument (TG, Labsys Evo, France) from 20 to 800 °C in air at a heating rate of 10 °C min^{-1}. The morphology of the samples was examined using field-emission SEM (Nova Nano230, Japan) and HRTEM (TECNAI G2 F30, USA). The Brunauer−Emmett−Teller measurements were carried out by N$_2$ isothermal adsorption using a compact specific surface area and pore size analyzer (BELSORP-Mini-II, Japan).

4.3. Electrochemical Measurements.
Electrochemical measurements of the samples were conducted using a CR2016 coin cell, which were assembled in an argon-filled glove box (Mikrouna Super 2440/750). Lithium metal was used as the counter electrode. A Celgard 2300 microporous polypropylene membrane was used as the separator. The working electrode was fabricated by mixing the active materials, acetylene black and PVDF at a weight proportion of 8:1:1 using NMP as the dispersing agent to form a uniform slurry. Then, the slurry was spread evenly on a copper foil substrate and dried at 80 °C in vacuum overnight. The loading mass of the active material is about 1 mg·cm^{-2}. The electrolyte was 1.0 M LiPF$_6$ solved in a mixture of ethylene carbonate and dimethylcarbonate (1:1 in volume). CV studies were carried out in the potential window of 0.01−3.0 V at a scan rate of 0.1 mV·s^{-1} on an electrochemical workstation (CHI 660E, China). Galvanostatic measurements were performed at different current rates between 0.01 and 3.0 V versus Li$^+$/Li on a battery tester (LAND, CT2001A, China). EIS measurements were carried out on an electrochemical workstation (Autolab PGSTA302N, Switzerland) at open circuit potential in the sweeping frequency range of 0.01−10 MHz by applying an ac signal of 5 mV in amplitude throughout the test. All the above measurements were carried out at ambient temperature.

■ ASSOCIATED CONTENT

Ⓢ Supporting Information

The Supporting Information is available free of charge on the ACS Publications website at DOI: 10.1021/acsomega.9b03026.

XPS analyses and SEM images of original rice husk (PDF)

■ AUTHOR INFORMATION

Corresponding Authors
*E-mail: bing.wu@esrf.fr (B.W.).
*E-mail: zhandan@hbuas.edu.cn (D.Z.).

ORCID ⦿
Heinz-Bernhard Kraatz: 0000-0002-7149-0110
Dermot F. Brougham: 0000-0002-1270-8415
André J. Simpson: 0000-0002-8247-5450
Bing Wu: 0000-0002-2739-5124

Notes
The authors declare no competing financial interest.

■ REFERENCES

(1) Ma, Y.; Hou, C.; Zhang, H.; Zhang, Q.; Liu, H.; Wu, S.; Guo, Z. Three-dimensional core-shell Fe_3O_4/Polyaniline coaxial heterogeneous nanonets: Preparation and high performance supercapacitor electrodes. *Electrochim. Acta* **2019**, *315*, 114−123.

(2) Zhang, Y.; An, Y.; Wu, L.; Chen, H.; Li, Z.; Dou, H.; Murugadoss, V.; Fan, J.; Zhang, X.; Mai, X.; Guo, Z. Metal-free energy storage systems: combining batteries with capacitors based on a methylene blue functionalized graphene cathode. *J. Mater. Chem. A* **2019**, *7*, 19668−19675.

(3) Nitta, N.; Wu, F.; Lee, J. T.; Yushin, G. Li-ion battery materials: present and future. *Mater. Today* **2015**, *18*, 252−264.

(4) Zhang, W.-J. A review of the electrochemical performance of alloy anodes for lithium-ion batteries. *J. Power Sources* **2011**, *196*, 13−24.

(5) Kaskhedikar, N. A.; Maier, J. Lithium Storage in Carbon Nanostructures. *Adv. Mater.* **2009**, *21*, 2664−2680.

(6) Poizot, P.; Laruelle, S.; Grugeon, S.; Dupont, L.; Tarascon, J.-M. Nano-sized transition-metal oxides as negative-electrode materials for lithium-ion batteries. *Nature* **2000**, *407*, 496−499.

(7) Taberna, P. L.; Mitra, S.; Poizot, P.; Simon, P.; Tarascon, J.-M. High rate capabilities Fe_3O_4-based Cu nano-architectured electrodes for lithium-ion battery applications. *Nat. Mater.* **2006**, *5*, 567−573.

(8) Cui, L.-F.; Yang, Y.; Hsu, C.-M.; Cui, Y. Carbon-Silicon Core-Shell Nanowires as High Capacity Electrode for Lithium Ion Batteries. *Nano Lett.* **2009**, *9*, 3370−3374.

(9) Sheng, L.; Jiang, H.; Liu, S.; Chen, M.; Wei, T.; Fan, Z. Nitrogen-doped carbon-coated MnO nanoparticles anchored on interconnected graphene ribbons for high-performance lithium-ion batteries. *J. Power Sources* **2018**, *397*, 325−333.

(10) Liu, B.; Zhang, Q.; Jin, Z.; Zhang, L.; Li, L.; Gao, Z.; Wang, C.; Xie, H.; Su, Z. Uniform Pomegranate-Like Nanoclusters Organized by Ultrafine Transition Metal Oxide@Nitrogen-Doped Carbon Subunits with Enhanced Lithium Storage Properties. *Adv. Energy Mater.* **2018**, *8*, 1702347.

(11) Hou, C.; Tai, Z.; Zhao, L.; Zhai, Y.; Hou, Y.; Fan, Y.; Dang, F.; Wang, J.; Liu, H. High performance MnO@C microcages with a hierarchical structure and tunable carbon shell for efficient and durable lithium storage. *J. Mater. Chem. A* **2018**, *6*, 9723−9736.

(12) Reddy, M. V.; Subba Rao, G. V.; Chowdari, B. V. R. Metal Oxides and Oxysalts as Anode Materials for Li Ion Batteries. *Chem. Rev.* **2013**, *113*, 5364−5457.

(13) Zhi, M.; Xiang, C.; Li, J.; Li, M.; Wu, N. Nanostructured carbon-metal oxide composite electrodes for supercapacitors: a review. *Nanoscale* **2013**, *5*, 72−88.

(14) Godshall, N. A.; Raistrick, I. D.; Huggins, R. A. Thermodynamic Investigations of Ternary Lithium-Transition Metal-Oxygen Cathode Materials. *Mater. Res. Bull.* **1980**, *15*, 561−570.

(15) Yue, J.; Gu, X.; Chen, L.; Wang, N.; Jiang, X.; Xu, H.; Yang, J.; Qian, Y. General synthesis of hollow MnO_2, Mn_3O_4 and MnO nanospheres as superior anode materials for lithium ion batteries. *J. Mater. Chem. A* **2014**, *2*, 17421−17426.

(16) Xu, G.-L.; Xu, Y.-F.; Sun, H.; Fu, F.; Zheng, X.-M.; Huang, L.; Li, J.-T.; Yang, S.-H.; Sun, S.-G. Facile synthesis of porous MnO/C nanotubes as a high capacity anode material for lithium ion batteries. *Chem. Commun.* **2012**, *48*, 8502−8504.

(17) Lai, F.; Zhang, X.; Wu, Q.; Zhang, J.; Li, Q.; Huang, Y.; Liao, Z.; Wang, H. Effect of Surface Modification with Spinel $NiFe_2O_4$ on Enhanced Cyclic Stability of $LiMn_2O_4$ Cathode Material in Lithium Ion Batteries. *ACS Sustain. Chem. Eng.* **2018**, *6*, 570−578.

(18) Di Lecce, D.; Andreotti, P.; Boni, M.; Gasparro, G.; Rizzati, G.; Hwang, J.-Y.; Sun, Y.-K.; Hassoun, J. Multiwalled Carbon Nanotubes Anode in Lithium-Ion Battery with $LiCoO_2$, $Li[Ni_{1/3}Co_{1/3}Mn_{1/3}]O_2$, and $LiFe_{1/4}Mn_{1/2}Co_{1/4}PO_4$ Cathodes. *ACS Sustain. Chem. Eng.* **2018**, *6*, 3225−3232.

(19) Cai, Z.; Xu, L.; Yan, M.; Han, C.; He, L.; Hercule, K. M.; Niu, C.; Yuan, Z.; Xu, W.; Qu, L.; Zhao, K.; Mai, L. Manganese Oxide/Carbon Yolk-Shell Nanorod Anodes for High Capacity Lithium Batteries. *Nano Lett.* **2015**, *15*, 738−744.

(20) Ding, Y.; Du, J.; Guo, L.; Zhou, H.; Yang, H.; Feng, W. Nanoscale MnO and natural graphite hybrid materials as high-performance anode for lithium ion batteries. *Electrochim. Acta* **2015**, *170*, 9−15.

(21) Sun, X.; Xu, Y.; Ding, P.; Chen, G.; Zheng, X.; Zhang, R.; Li, L. The composite sphere of manganese oxide and carbon nanotubes as a prospective anode material for lithium-ion batteries. *J. Power Sources* **2014**, *255*, 163−169.

(22) Zheng, F.; Yin, Z.; Xia, H.; Bai, G.; Zhang, Y. Porous MnO@C nanocomposite derived from metal-organic frameworks as anode materials for long-life lithium-ion batteries. *Chem. Eng. J.* **2017**, *327*, 474−480.

(23) Zhang, C.; Wang, J.-G.; Jin, D.; Xie, K.; Wei, B. Facile fabrication of MnO/C core-shell nanowires as an advanced anode material for lithium-ion batteries. *Electrochim. Acta* **2015**, *180*, 990−997.

(24) Cao, Y.; Xiao, L.; Wang, W.; Choi, D.; Nie, Z.; Yu, J.; Saraf, L. V.; Yang, Z.; Liu, J. Reversible Sodium Ion Insertion in Single Crystalline Manganese Oxide Nanowires with Long Cycle Life. *Adv. Mater.* **2011**, *23*, 3155−3160.

(25) Xu, Y.-F.; Xu, G.-L.; Su, H.; Chen, Y.; Fang, J.-C.; Wang, Q.; Huang, L.; Li, J.-T.; Sun, S.-G. Porous MnO/C of composite nanostructure consisting of nanorods and nano-octahedra as anode of lithium ion batteries with enhanced electrochemical performances. *J. Alloys Compd.* **2016**, *676*, 156−163.

(26) Xiao, Y.-C.; Xu, C.-Y.; Sun, X.-Y.; Pei, Y.; Wang, P.-P.; Ma, F.-X.; Zhen, L. Constructing yolk-shell MnO@C nanodiscs through a carbothermal reduction process for highly stable lithium storage. *Chem. Eng. J.* **2018**, *336*, 427−435.

(27) Kalderis, D.; Bethanis, S.; Paraskeva, P.; Diamadopoulos, E. Production of activated carbon from bagasse and rice husk by a single-stage chemical activation method at low retention times. *Bioresour. Technol.* **2008**, *99*, 6809−6816.

(28) Soltani, N.; Bahrami, A.; Pech-Canul, M. I.; González, L. A. Review on the physicochemical treatments of rice husk for production of advanced materials. *Chem. Eng. J.* **2015**, *264*, 899−935.

(29) Galhardo, T. S.; Simone, N.; Gonçalves, M.; Figueiredo, F. C. A.; Mandelli, D.; Carvalho, W. A. Preparation of Sulfonated Carbons from Rice Husk and Their Application in Catalytic Conversion of Glycerol. *ACS Sustain. Chem. Eng.* **2013**, *1*, 1381−1389.

(30) Chen, Y.; Zhu, Y.; Wang, Z.; Li, Y.; Wang, L.; Ding, L.; Gao, X.; Ma, Y.; Guo, Y. Application studies of activated carbon derived from

rice husks produced by chemical-thermal process-A review. *Adv. Colloid Interface* **2011**, *163*, 39−52.

(31) Sun, L.; Gong, K. Silicon-based materials from rice husks and their applications. *Ind. Eng. Chem. Res.* **2001**, *40*, 5861−5877.

(32) Prabunathan, P.; Sethuraman, K.; Alagar, M. MnO$_2$-doped, polyaniline-grafted rice husk ash nanocomposites and their electrochemical capacitor applications. *RSC Adv.* **2014**, *4*, 47726−47734.

(33) Zhang, L.; Liu, Z.; Cui, G.; Chen, L. Biomass-derived materials for electrochemical energy storages. *Prog. Polym. Sci.* **2015**, *43*, 136−164.

(34) Ling, Z.; Wang, Z.; Zhang, M.; Yu, C.; Wang, G.; Dong, Y.; Liu, S.; Wang, Y.; Qiu, J. Sustainable Synthesis and Assembly of Biomass-Derived B/N Co-Doped Carbon Nanosheets with Ultrahigh Aspect Ratio for High-Performance Supercapacitors. *Adv. Funct. Mater.* **2016**, *26*, 111−119.

(35) Li, Y.; Xu, S.; Wu, X.; Yu, J.; Wang, Y.; Hu, Y.-S.; Li, H.; Chen, L.; Huang, X. Amorphous monodispersed hard carbon microspherules derived from biomass as a high performance negative electrode material for sodium-ion batteries. *J. Mater. Chem. A* **2015**, *3*, 71−77.

(36) Xiang, C.; Liu, Y.; Yin, Y.; Huang, P.; Zou, Y.; Fehse, M.; She, Z.; Xu, F.; Banerjee, D.; Hermida Merino, D.; Longo, A.; Kraatz, H.-B.; Brougham, D. F.; Wu, B.; Sun, L. Facile Green Route to Ni/Co Oxide Nanoparticle Embedded 3D Graphitic Carbon Nanosheets for High Performance Hybrid Supercapacitor Devices. *ACS Appl. Energy Mater.* **2019**, *2*, 3389−3399.

(37) Liu, D.; Zhang, W.; Lin, H.; Li, Y.; Lu, H.; Wang, Y. Hierarchical porous carbon based on the self-templating structure of rice husk for high-performance supercapacitors. *RSC Adv.* **2015**, *5*, 19294−19300.

(38) Yuan, C.; Lin, H.; Lu, H.; Xing, E.; Zhang, Y.; Xie, B. Synthesis of hierarchically porous MnO$_2$/rice husks derived carbon composite as high-performance electrode material for supercapacitors. *Appl. Energy* **2016**, *178*, 260−268.

(39) Khalili, N. R.; Campbell, M.; Sandi, G.; Golaś, J. Production of micro- and mesoporous activated carbon from paper mill sludge - I. Effect of zinc chloride activation. *Carbon* **2000**, *38*, 1905−1915.

(40) He, X.; Ling, P.; Yu, M.; Wang, X.; Zhang, X.; Zheng, M. Rice husk-derived porous carbons with high capacitance by ZnCl$_2$ activation for supercapacitors. *Electrochim. Acta* **2013**, *105*, 635−641.

(41) Deng, L.; Zhong, W.; Wang, J.; Zhang, P.; Fang, H.; Yao, L.; Liu, X.; Ren, X.; Li, Y. The enhancement of electrochemical capacitance of biomass-carbon by pyrolysis of extracted nanofibers. *Electrochim. Acta* **2017**, *228*, 398−406.

(42) Baddour-Hadjean, R.; Pereira-Ramos, J.-P. Raman Microspectrometry Applied to the Study of Electrode Materials for Lithium Batteries. *Chem. Rev.* **2010**, *110*, 1278−1319.

(43) Choi, H. C.; Jung, Y. M.; Kim, S. B. Size effects in the Raman spectra of TiO$_2$ nanoparticles. *Vib. Spectrosc.* **2005**, *37*, 33−38.

(44) Li, K.; Shua, F.; Guo, X.; Xue, D. High performance porous MnO@C composite anode materials for lithium-ion batteries. *Electrochim. Acta* **2016**, *188*, 793−800.

(45) Thommes, M.; Kaneko, K.; Neimark, A. V.; Olivier, J. P.; Rodriguez-Reinoso, F.; Rouquerol, J.; Sing, K. S. W. Physisorption of gases, with special reference to the evaluation of surface area and pore size distribution (IUPAC Technical Report). *Pure Appl. Chem.* **2015**, *87*, 1051−1069.

(46) Caturla, F.; Molina-Sabio, M.; Rodríguez-Reinoso, F. Preparation of Activated Carbon by Chemical Activation with Zncl$_2$. *Carbon* **1991**, *29*, 999−1007.

(47) Tang, D.; Luo, Y.; Lei, W.; Xiang, Q.; Ren, W.; Song, W.; Chen, K.; Sun, J. Hierarchical porous carbon materials derived from waste lentinus edodes by a hybrid hydrothermal and molten salt process for supercapacitor applications. *Appl. Surf. Sci.* **2018**, *462*, 862−871.

(48) Xia, P.; Lin, H. B.; Tu, W. Q.; Chen, X. Q.; Cai, X.; Zheng, X. W.; Xu, M. Q.; Li, W. S. A Novel Fabrication for Manganese Monoxide/Reduced Graphene Oxide Nanocomposite as High Performance Anode of Lithium Ion Battery. *Electrochim. Acta* **2016**, *198*, 66−76.

(49) Fehse, M.; Sougrati, M. T.; Darwiche, A.; Gabaudan, V.; La Fontaine, C.; Monconduit, L.; Stievano, L. Elucidating the origin of superior electrochemical cycling performance: new insights on sodiation-desodiation mechanism of SnSb from operando spectroscopy. *J. Mater. Chem. A* **2018**, *6*, 8724−8734.

(50) Cabana, J.; Monconduit, L.; Larcher, D.; Palacín, M. R. Beyond Intercalation-Based Li-Ion Batteries: The State of the Art and Challenges of Electrode Materials Reacting Through Conversion Reactions. *Adv. Mater.* **2010**, *22*, No. E170.

(51) Xia, Y.; Xiao, Z.; Dou, X.; Huang, H.; Lu, X.; Yan, R.; Gan, Y.; Zhu, W.; Tu, J.; Zhang, W.; Tao, X. Green and Facile Fabrication of Hollow Porous MnO/C Microspheres from Microalgaes for Lithium-Ion Batteries. *ACS Nano* **2013**, *7*, 7083−7092.

(52) Huang, X. H.; Tu, J. P.; Zhang, C. Q.; Chen, X. T.; Yuan, Y. F.; Wu, H. M. Spherical NiO-C composite for anode material of lithium ion batteries. *Electrochim. Acta* **2007**, *52*, 4177−4181.

(53) Jiang, H.; Hu, Y.; Guo, S.; Yan, C.; Lee, P. S.; Li, C. Rational Design of MnO/Carbon Nanopeapods with Internal Void Space for High-Rate and Long-Life Li-Ion Batteries. *ACS Nano* **2014**, *8*, 6038−6046.

(54) Luo, W.; Hu, X.; Sun, Y.; Huang, Y. Controlled Synthesis of Mesoporous MnO/C Networks by Microwave Irradiation and Their Enhanced Lithium-Storage Properties. *ACS Appl. Mater. Interfaces* **2013**, *5*, 1997−2003.

(55) Zhang, X.; Xing, Z.; Wang, L.; Zhu, Y.; Li, Q.; Liang, J.; Yu, Y.; Huang, T.; Tang, K.; Qian, Y.; Shen, X. Synthesis of MnO@C core-shell nanoplates with controllable shell thickness and their electrochemical performance for lithium-ion batteries. *J. Mater. Chem.* **2012**, *22*, 17864−17869.

(56) Zheng, J. M.; Engelhard, M. H.; Mei, D. H.; Jiao, S. H.; Polzin, B. J.; Zhang, J. G.; Xu, W. Electrolyte additive enabled fast charging and stable cycling lithium metal batteries. *Nat. Energy* **2017**, *2*, 17012.

(57) Elmouwahidi, A.; Bailón-García, E.; Castelo-Quibén, J.; Pérez-Cadenas, A. F.; Maldonado-Hódar, F. J.; Carrasco-Marín, F. Carbon-TiO$_2$ composites as high-performance supercapacitor electrodes: synergistic effect between carbon and metal oxide phases. *J. Mater. Chem. A* **2018**, *6*, 633−644.

(58) Zhang, S.; Zheng, M.; Lin, Z.; Li, N.; Liu, Y.; Zhao, B.; Pang, H.; Cao, J.; He, P.; Shi, Y. Activated carbon with ultrahigh specific surface area synthesized from natural plant material for lithium-sulfur batteries. *J. Mater. Chem. A* **2014**, *2*, 15889−15896.

(59) Bijelic, M.; Liu, X.; Sun, Q.; Djurisic, A. B.; Xie, M. H.; Ng, A. M. C.; Suchomski, C.; Djerdj, I.; Skoko, Z.; Popovic, J. Long cycle life of CoMn$_2$O$_4$ lithium ion battery anodes with high crystallinity. *J. Mater. Chem. A* **2015**, *3*, 14759−14767.

(60) Barchasz, C.; Leprêtre, J.-C.; Alloin, F.; Patoux, S. New insights into the limiting parameters of the Li/S rechargeable cell. *J. Power Sources* **2012**, *199*, 322−330.

(61) Wang, L.; Yan, J.; Xu, Z.; Wang, W.; Wen, J.; Bai, X. Rate mechanism of vanadium oxide coated tin dioxide nanowire electrode for lithium ion battery. *Nano Energy* **2017**, *42*, 294−299.

(62) Zhang, L. L.; Zhao, X. S. Carbon-based materials as supercapacitor electrodes. *Chem. Soc. Rev.* **2009**, *38*, 2520−2531.

(63) Barai, A.; Chouchelamane, G. H.; Guo, Y.; McGordon, A.; Jennings, P. A study on the impact of lithium-ion cell relaxation on electrochemical impedance spectroscopy. *J. Power Sources* **2015**, *280*, 74−80.

(64) Osaka, T.; Mukoyama, D.; Nara, H. Review-Development of Diagnostic Process for Commercially Available Batteries, Especially Lithium Ion Battery, by Electrochemical Impedance Spectroscopy. *J. Electrochem. Soc.* **2015**, *162*, A2529−A2537.

(65) Xu, C.; Manukyan, K. V.; Adams, R. A.; Pol, V. G.; Chen, P.; Varma, A. One-step solution combustion synthesis of CuO/Cu$_2$O/C anode for long cycle life Li-ion batteries. *Carbon* **2019**, *142*, 51−59.

(66) Zhu, Z.; Cheng, F.; Chen, J. Investigation of effects of carbon coating on the electrochemical performance of Li$_4$Ti$_5$O$_{12}$/C nanocomposites. *J. Mater. Chem. A* **2013**, *1*, 9484−9490.

(67) Xiao, Z.; Chen, W. W.; Liu, K.; Cui, P.; Zhan, D. Porous Biomass Carbon Derived from Peanut Shells as Electrode Materials

with Enhanced Electrochemical Performance for Supercapacitors. *Int. J. Electrochem. Sci.* **2018**, *13*, 5370−5381.

(68) Cui, Z.; Liu, Q.; Xu, C.; Zou, R.; Zhang, J.; Zhang, W.; Guan, G.; Hu, J.; Sun, Y. A new strategy to effectively alleviate volume expansion and enhance the conductivity of hierarchical MnO@C nanocomposites for lithium ion batteries. *J. Mater. Chem. A* **2017**, *5*, 21699−21708.

(69) Chen, T.; Wu, Z.; Xiang, W.; Wang, E.; Chen, T.; Guo, X.; Chen, Y.; Zhong, B. Cauliflower-like MnO@C/N composites with multiscale, expanded hierarchical ordered structures as electrode materials for Lithium- and Sodium-ion batteries. *Electrochim. Acta* **2017**, *246*, 931−940.

(70) Cao, Z.; Shi, M.; Ding, Y.; Zhang, J.; Wang, Z.; Dong, H.; Yin, Y.; Yang, S. Lotus-Root-Like MnO/C Hybrids as Anode Materials for High Performance Lithium-Ion Batteries. *J. Phys. Chem. C* **2017**, *121*, 2546−2555.

(71) Kang, D.; Liu, Q.; Si, R.; Gu, J.; Zhang, W.; Zhang, D. Crosslinking-derived MnO/carbon hybrid with ultrasmall nanoparticles for increasing lithium storage capacity during cycling. *Carbon* **2016**, *99*, 138−147.

(72) Zhu, W.; Huang, H.; Zhang, W.; Tao, X.; Gan, Y.; Xia, Y.; Yang, H.; Guo, X. Synthesis of MnO/C composites derived from pollen template for advanced lithium-ion batteries. *Electrochim. Acta* **2015**, *152*, 286−293.

(73) Sun, B.; Chen, Z.; Kim, H.-S.; Ahn, H.; Wang, G. MnO/C core-shell nanorods as high capacity anode materials for lithium-ion batteries. *J. Power Sources* **2011**, *196*, 3346−3349.